Convection Initiation Associated With Ambient Winds and Local Circulations Over a Tropical Island in South China

Lei Zhu[1] , **Lanqiang Bai[2,3]** , **Guixing Chen[2]** , **Y. Qiang Sun[4]** , and **Zhiyong Meng[5]**

[1]Key Laboratory of Meteorological Disaster (KLME), Ministry of Education and Collaborative Innovation Center on Forecast and Evaluation of Meteorological Disasters (CIC-FEMD), Nanjing University of Information Science and Technology, Nanjing, China, [2]School of Atmospheric Sciences, Sun Yat-sen University, and Southern Marine Science and Engineering Guangdong Laboratory (Zhuhai), Zhuhai, China, [3]Foshan Tornado Research Center, Foshan Meteorological Service, Foshan, China, [4]Atmospheric and Oceanic Sciences Program, Princeton University, Princeton, NJ, USA, [5]Department of Atmospheric and Oceanic Sciences, School of Physics, Peking University, Beijing, China

Abstract Convection is highly active on tropical islands. Based on a 3-year radar climatology over Hainan Island, a mountainous tropical island in South China, we identified a distinct spatial dependence of convection initiation (CI) on the speed of the large-scale low-level flow. Convection initiates most prominently over the lee-side plains in high-wind conditions while over mountains in low-wind conditions. Quasi-idealized numerical simulations suggest that mountain ridges stimulate the formation and growth of horizontal convective rolls (HCRs) over the lee-side plains in high-wind conditions. These HCRs subsequently intersect with sea-breeze fronts, which enhances the low-level convergence favoring CI on the lee-side plains of the island. During low-wind conditions, thermally driven circulations control and favor CI over the mountains during the day. The findings highlight that the response of local circulations to the lower-troposphere ambient flow and diurnal thermal heating is an important aspect of convection initiation on the island.

Plain Language Summary Skillfully predicting the location and timing of the formation of thunderstorms in the tropics is a challenging problem. Using radar observations, this study investigates how the key characteristics of low-level winds influence the formation of thunderstorms on a mountainous tropical island (Hainan Island in South China). Modeling results demonstrate that the spatial occurrence of the thunderstorm formation is sensitive to the speed of low-level winds. The thunderstorm formation occurs most prominently on the downwind plains and over the upwind mountain regions under the high-wind and low-wind conditions, respectively. During the high-wind condition, the perturbed ambient flows downwind of ridges help to enhance the convergence in the boundary layer, and thus contribute to the thunderstorm formation in the plain region in the afternoon. Under low-wind conditions, the local daytime heating is responsible for the frequent formation of thunderstorms over mountains. Considering that large-scale circulations can be predicted reasonably well by numerical models, the findings of this study may assist operational forecasts of the formation of thunderstorms on tropical islands.

1. Introduction

One of the most challenging aspects of severe weather forecasting is to predict when and where a convective storm will develop, also known as convection initiation (CI). CI is commonly deemed to have occurred when the first radar echo of a convective storm appears. It is usually the result of multiscale interactions between large-scale atmospheric circulations, local circulations, and the terrain (Wilson & Roberts, 2006). The forecast errors regarding CI timing and location are two of the major factors that limit the predictability of subsequent severe weather and quantitative precipitation forecasts (Weckwerth et al., 2011). Improving our understanding of CI mechanisms would be of great help for disaster prevention and mitigation.

Convection over tropical islands is particularly active, which makes tropical islands among the rainiest regions on Earth (Carbone et al., 2000). In the presence of moisture pooling and instability, the locally enhanced lift associated with boundary-layer convergence zones, such as sea-breeze fronts (SBFs) and
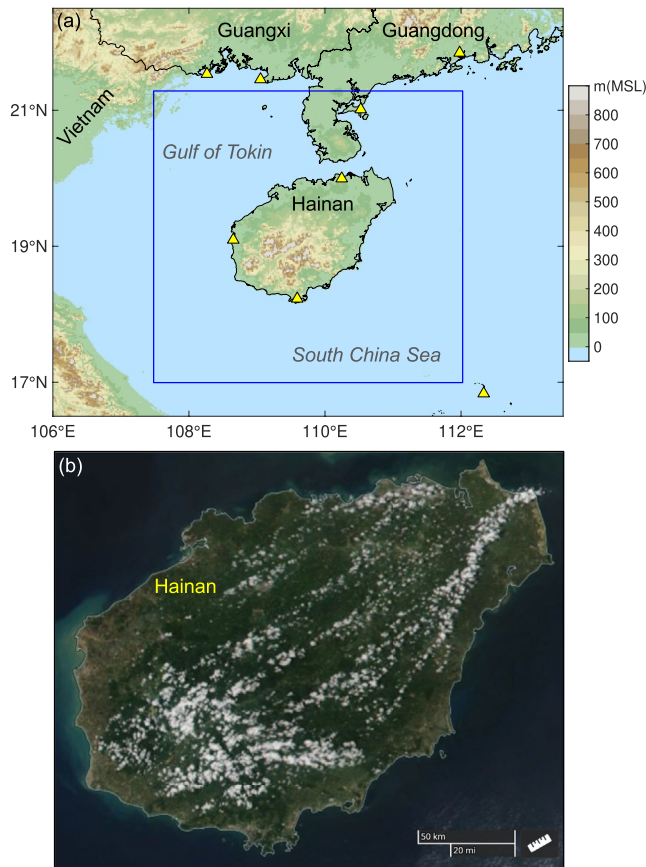
Figure 1. (a) Terrain height (shaded) with weather radar sites (triangles). The blue box indicates the WRF domain described in the text. (b) Snapshot of satellite imagery on June 03, 2016 obtained from the NASA WorldView website at https://worldview.earthdata.nasa.gov/.

the leading edges of cold pools (i.e., gust fronts), is often the precursor to CI (e.g., Kingsmill, 1995; Wilson & Roberts, 2006). Previous studies have demonstrated that sea-breeze dynamics greatly influence the convective activity over tropical islands (e.g., Bennett et al., 2006; Carbone et al., 2000). CI on islands often takes place at the time of or prior to the collision of SBFs with horizontal convective rolls (HCRs) in response to daytime surface heating (Fovell, 2005; Fovell & Dailey, 2001). Previous studies have suggested that the movement of SBFs can be strongly modulated by large-scale circulations, and thus impact the subsequent CI and convective development (Chen et al., 2017; Miller et al., 2003; Qian et al., 2013; Simpson, 1994; Zhu et al., 2020). Building upon existing connections between CI and local circulations, an improved understanding of CI under different conditions of large-scale atmospheric circulations may aid in the operational forecasts of severe weather over tropical islands.

Located to the south of mainland China, Hainan Island (roughly at 19°N, 110°E as shown in Figure 1a) is a "natural convection laboratory," primed to study convective processes over tropical islands. It is characterized by plains in the northeast and mountains in the southwest with a peak altitude of ~1.8 km above mean sea level (Figure 1a). Strongly affected by the East Asian summer monsoon, Hainan Island is the most CI-prone region in South China (Bai et al., 2020a). The annual precipitation amount usually reaches 1,000 mm, even exceeding 2,500 mm in some years (Wang, 2014). The frequently occurring convective storms and the associated high winds and precipitation greatly impact the agriculture over this island which extensively cultivates paddy rice and various tropical fruits (Chen et al., 2018; Zhang et al., 2017; Zheng et al., 2016). The island storms are demonstrated to be particularly active when this area is dominated by low-level southwesterlies (Bai et al., 2020a). Under such atmospheric circulations, a significant diurnal cycle of storms occurs in the afternoon attributable to the collision of the SBFs from different sides of the island (Zhu et al., 2017, 2020). Prior studies have suggested that the development of local circulations (e.g., SBFs, HCRs, mountain waves) can also be dramatically influenced by the ambient flows (e.g., Bennett et al., 2006; Chen et al., 2016; Fovell & Dailey, 2001; Qian et al., 2009). Consequently, a tropical island such as Hainan is an ideal place to study the impacts of local circulations on CI activity under different prevailing ambient flows.

The goal of this work is to investigate the dependence of CI characteristics and the associated local circulations on the speed of the prevailing lower-troposphere flow over the tropical island in South China. The data and methods for the CI statistics are described in Section 2. The spatial patterns of CI during the high-wind and low-wind conditions are presented in Section 3. Analysis of the low-level lifting for CI based on the numerical simulations and a brief summary are given in Sections 4 and 5, respectively.

2. Methods

2.1. Observational Data Set and CI Identification

The observational data based on mosaics of radar reflectivity were used to identify the CI occurrence around Hainan Island. Through compositing the basic reflectivity of multiple operational weather radars in South China, the radar mosaics help to monitor weather systems at a large horizontal spatial scale. In this study, the radar reflectivity was retrieved from the radar mosaic maps that were created in real-time by the National Meteorological Center of China Meteorological Administration. These radar mosaic maps were generated every 10 min before June 15, 2016 and 6 min afterward (Bai et al., 2020b). The horizontal spatial resolution of the reflectivity data is ~2.15 km. A CI event was determined when a first-occurrence convective cell satisfied the criteria described in Bai et al. (2020b) in which the CI detection methods were adapted from

Fabry et al. (2013). Here, a convective cell was defined as the radar echoes (≥40 dBZ) that consisted of at least two connected pixels to eliminate some possibly invalid convection. For more details regarding the CI identification, please refer to Bai et al. (2020b).

To avoid the influence of tropical cyclones, we focused the study period on the first rainy season (April-June) in South China from 2016 to 2018. Only the days with low-level southwesterlies were selected for analysis in order to keep the synoptic circulations consistent with the prevailing mean flows (Zhu et al., 2020). Specifically, the selected days were determined when the domain-averaged (refer to the blue rectangle in Figure 1a) daily mean 850-hPa horizontal winds have a direction between 200° and 250° using the ERA-Interim reanalysis. The obtained 147 days were then separated into three groups based on the averaged wind speed, namely high-wind days (top 30%; 8.3–15.6 m s^{-1}), moderate-wind days (middle 40%; 5.1–8.3 m s^{-1}) and low-wind days (the rest 30%; 0.9–5.1 m s^{-1}), respectively. Only the high-wind and low-wind groups were used to investigate the dependence of CI on the low-level wind speeds of large-scale background flows.

2.2. Numerical Model Setup

Numerical simulations were also conducted to investigate the impacts of the large-scale low-level wind speed on the CI activity over this tropical island. The numerical model utilized in this study was the fully compressible, nonhydrostatic WRF-ARW Model (Skamarock et al., 2008), version 3.8. One domain was applied covering an area of 450 km × 450 km at a horizontal grid spacing of 3 km (150 × 150 grid points; Figure 1a). The model topography is shown in Figure S1a for reference. In the vertical direction, 50 stretched-grid levels were configured with a nominal model top at 50 hPa. The physical parameterization schemes include the WRF single moment six-class (WSM6) microphysics (Hong et al., 2004), the Yonsei State University (YSU) PBL scheme (Noh et al., 2003), and the rapid radiative transfer model (RRTM) for longwave and shortwave radiation schemes (Chou & Suarez, 1994). No cumulus scheme was used.

A pair of 5-days full-physics simulations under the high-wind and low-wind conditions were initialized with the averaged 6-hourly ERA-Interim reanalysis data (refer to the CTL experiment described in Table S1). The initial and lateral boundary conditions (ICBCs) of the simulations were derived from the averaged ERA-Interim reanalysis at 0800, 1400, 2000, and 0200 LST (LST = UTC + 8 h) on the high-wind and low-wind days, respectively. The model was initiated at 0800 LST and the lateral boundary conditions for the following 4 days were cycled periodically in time (i.e., duplications of the averaged ERA-Interim reanalysis at 0800, 1400, 2000, and 0200 LST of the first day). Using such composites as ICBCs, the major patterns of large-scale circulations are maintained while transient atmospheric perturbations can be filtered out (e.g., Chen et al., 2017; Trier et al., 2010). Thermally driven diurnal activities such as land-sea-breeze circulations can repeatedly develop under such an averaged atmospheric environment (Bao & Zhang, 2013; Zhang et al., 2014; Zhu et al., 2017). For investigating the effects of orography and excluding the interference of moist convection, additional simulations without cloud microphysical processes and without terrain were conducted (refer to the DRY and DRY_NO_TER experiments described in Table S1).

3. Spatial Patterns of CI Over Hainan Island

3.1. Ground-Based Radar Observations

Figure 2 shows the daily frequency of CI occurrence derived from the radar observations. In both wind groups, two distinct CI hotspots are located in the northeast and southwest areas of the island, respectively. Over the northeast portion of the island, CI occurrences are particularly active on high-wind days (Figure 2a). CI frequently occurs from the mountain lees to the northeast coasts covering a large fraction of the plains. By contrast, the northeastern CI occurrences on low-wind days are concentrated in coastal regions (Figure 2b). Over the southwest portion of the island, the number and hotspots of CI occurrences are also different between the two groups. On low-wind days, CI preferentially occurs in mountain areas (Figure 2b). By contrast, a relatively small number of CI occurrences are concentrated on the southwest coasts on high-wind days (Figure 2a). The spatial pattern of CI occurrence on the island also shows diurnal distinctions. Convection primarily initiates during the daytime in both high-wind and low-wind groups (Figures 2c–2f). Only a small fraction of CI occurrences take place at night (Figures 2e and 2f). During
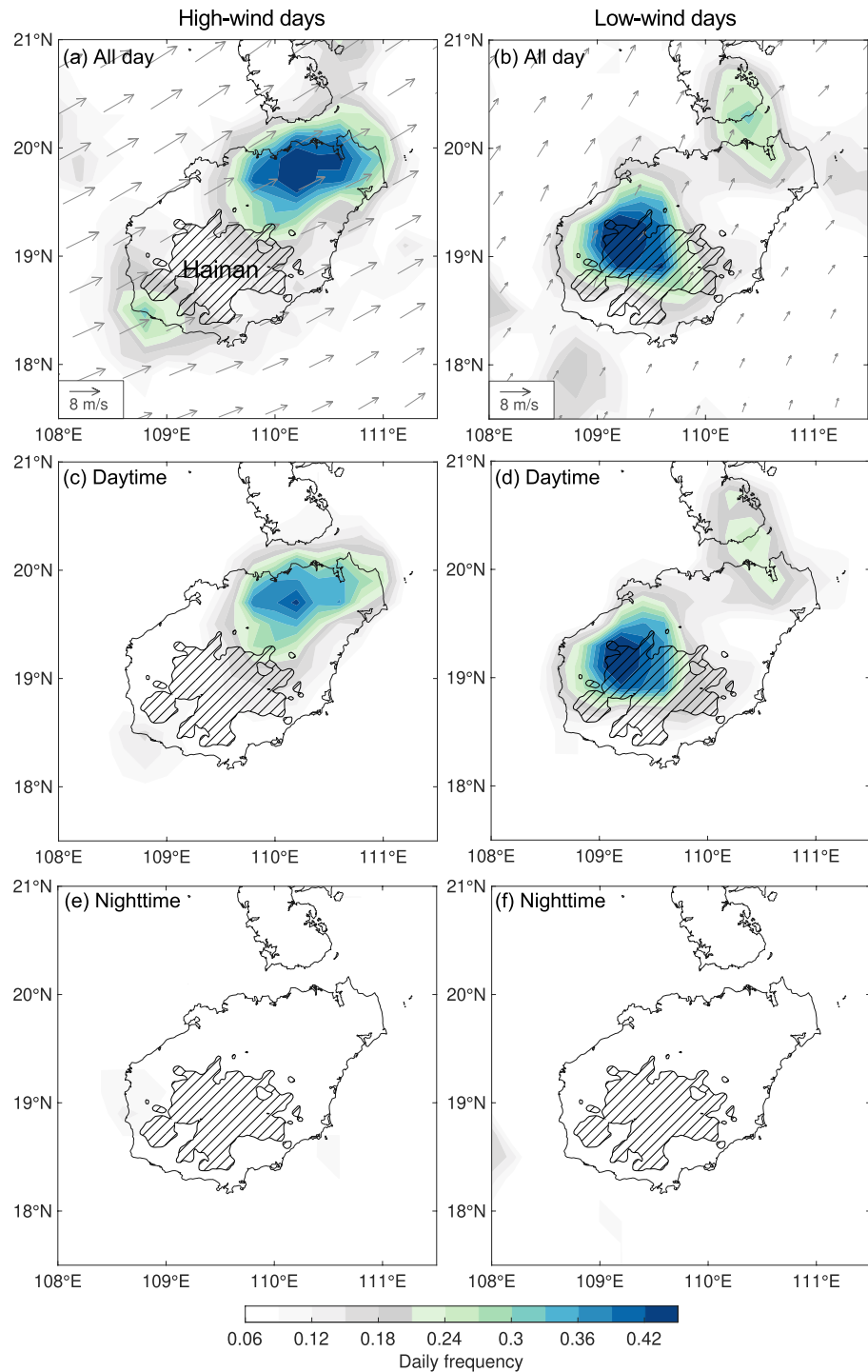
Figure 2. Daily frequency (shaded) of convection initiation (CI) occurrence during April-June from 2016 to 2018 grouped on (left) high-wind and (right) low-wind days. The hatched area within the contours indicates the terrain at an altitude of above 250 m. The 850-hPa horizontal winds (vectors) averaged on (a) high-wind and (b) low-wind days are also shown for reference.

daytime, the island is dominated by the plain-region CI in high-wind conditions (Figure 2c). However, the daytime CI on low-wind days presents a major hotspot in mountain areas and a minor hotspot near the northeast coasts (Figure 2d). Because the nocturnal CI in high-wind and low-wind conditions is overall inactive, this study focuses on the daytime CI on the island.

3.2. Quasi-Idealized Convection-Permitting Numerical Simulations

This section presents the results from the quasi-idealized convection-permitting simulations with the experimental design as described in Section 2.2. During the 5-days model integration, the temporal variations along the model lateral boundaries were constrained to be the same each day. Therefore, the daily simulated results tend to be analogous after the model reaches radiative convective equilibrium. For instance, the model integration becomes stable from day 2 and the simulated convective activities in the last four days are nearly the same (Figure S2). For this reason, the analysis will be performed based on the results of day 5.

Figure 3 shows the CI occurrences and the subsequent convection in the CTL simulations under high-wind and low-wind conditions, respectively. The spatial distributions of the simulated CI locations on the island (Figures 3a and 3b) generally agree well with the corresponding observed CI patterns (Figures 2c and 2d). In both simulations, convection first initiated at ~1300 LST. The initiated daytime convection during the high-wind condition is located on the northeast plains (Figures 3a, 3c and 3e). During the low-wind condition, the dominant convection primarily occurs over the southwest mountains (Figures 3b, 3d and 3f). A secondary simulated CI hotspot was also found on the northeast plain and coastal regions as revealed by the radar observations (Figures 2d and 2f). However, the convective echoes appearing in this area are generally weaker than those over the southwest mountains (Figures 3d and 3f). In addition to the convection occurrences, the simulated diurnal cycles of rainfall in the high-wind and low-wind conditions are generally in accordance with the observations (e.g., rain rate averaged on the island as shown in Figure S3). It is worth noting that the simulated convection barely initiates during nighttime hours primarily due to the limited instability in that time. The observed nighttime rainfall on the island mainly results from the nocturnal propagating precipitation systems from the Gulf of Tokin (Figure 1a).

4. Lifting for CI Under High-Wind and Low-Wind Conditions

The results of Section 3 suggest that the convection-permitting simulations exhibit a fairly good agreement with radar observations in regards to reproduce the spatial characteristics of CI under the high-wind and low-wind large-scale atmospheric environments. It is thus reasonable to further explore the regional lifting for CI with the aid of these simulations. The mesoscale lifting at low levels is often the most pivotal ingredient in triggering convection (Doswell et al., 1996; Weckwerth & Parsons, 2006). Figure 4a shows the maximum vertical motions in the lowest 2 km above ground level during the high-wind condition in the CTL experiment. Distinct thin-line features of updraft are identified in the early afternoon along the coastlines over the northeast part of the island, indicative of SBFs caused by the land-sea heating contrast (labeled N-SBF and S-SBF). After the passage of these SBFs, a sharp increase of near-surface specific humidity is captured (Figures S1a and S1b). The sea breezes are particularly strong during 1400–1700 LST when the island surface is substantially heated. In addition to the SBF features, several organized near-surface convergent zones extend from the lee side of the major ridges to the northeast coasts (denoted by the magenta arrows in Figure 4a). Some southwest-northeast-oriented convergent zones with weaker updrafts are also found over the flat terrain that are not located downwind of the major ridges (refer to the light-yellow bands denoted by the cyan arrows in Figure 4a).

In order to clarify the evolution of the local circulations, additional dry simulations (DRY in Table S1) in contrast to the aforementioned CTL simulations were conducted. The cloud microphysics were turned off and thus no latent heating or cooling processes are allowed (moisture was still included). The main difference between the DRY and CTL experiments is the presence of moist convection. For example, the regional dynamic fields are severely disturbed by cold outflows after the convection initiates in the CTL experiment (Figures S1c–S1e). By contrast, the dynamic fields are nearly the same in the CTL and DRY simulations at 1200 LST, ~1 h before the CI over the island (Figures 4a and 4b). This consistency of dynamic fields before CI gives us confidence to discuss the local circulations over Hainan Island based on the DRY simulations. Mountain waves, horizontal convective rolls, and sea breezes will stand out if the convectively induced influences (e.g., cold outflows) are excluded. The DRY experiments are thus helpful for a direct assessment of these lower-troposphere circulations (e.g., Weckwerth et al., 1997).

From the evolution of these thin-line features in the DRY experiment (Figures 4b–4f), the collision between N-SBF and S-SBF occurs from ~1200 LST on the northeast-end of the island and extends southwestward to
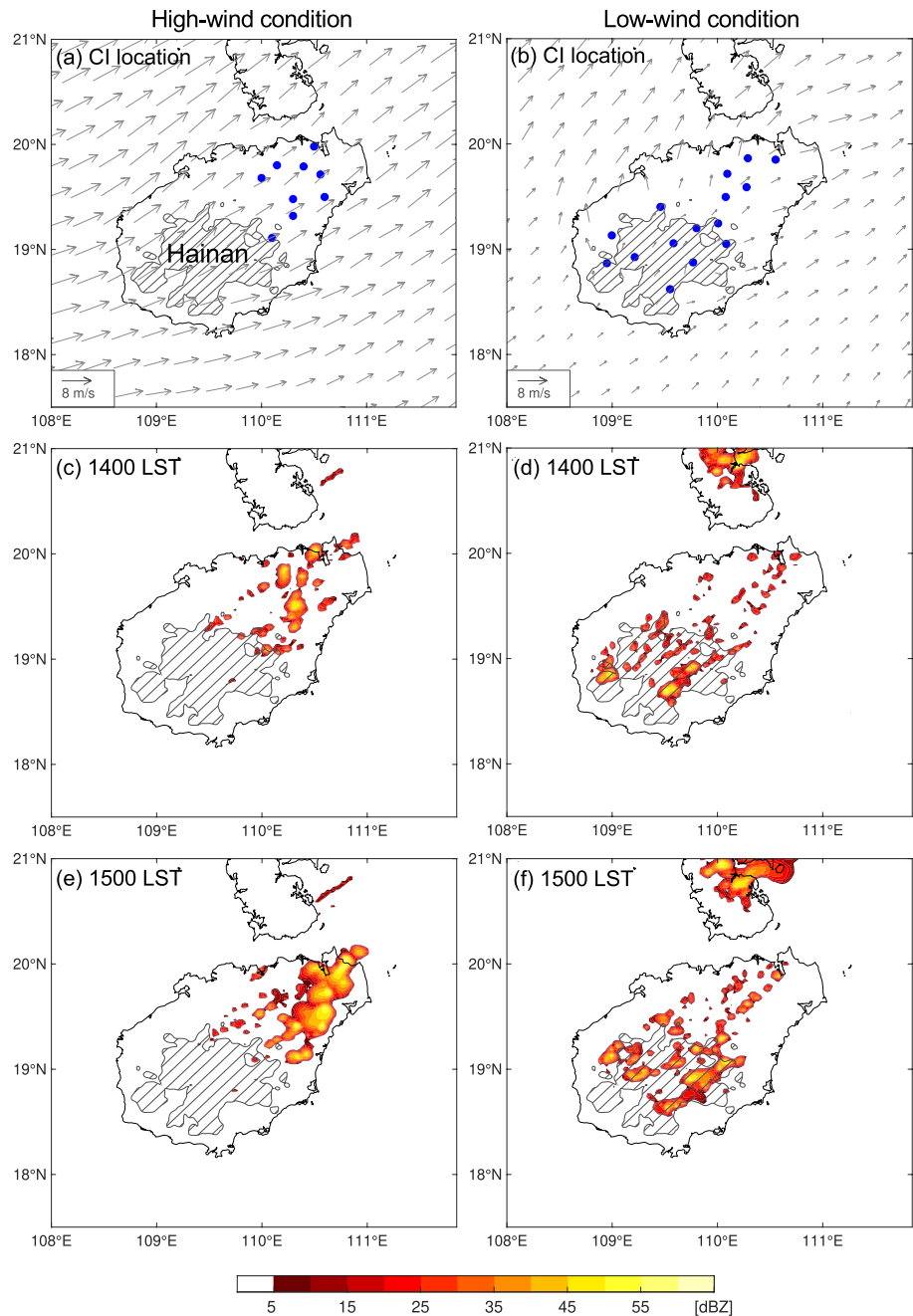
Figure 3. (a, b) Simulated convection initiation (CI) locations (blue dots) on Hainan Island and (c–f) the simulated composite radar reflectivity (shaded; units: dBZ) at different times in (left column) high-wind and (right column) low-wind conditions. The hatched area within the contours indicates the terrain at an altitude of above 250 m.

the plain regions. The resultant forced lifting is believed to be responsible for the daytime CI occurrences on the northeast coasts both in the high-wind and low-wind conditions (Figures 2c, 2d and 3a, 3b). It has long been known that the collision of such convergent boundaries is sometimes a precursor to CI, such as the frequent CI on the Florida peninsula and the Tiwi Islands (Boybeyi & Raman, 1992; Crook, 2001; Saito et al., 2001). The intersecting points of multiple convergent boundaries are common locations for CI (e.g., Bai et al., 2019; Weckwerth & Parsons, 2006).

Although the SBF collision occurs during both of the high-wind and low-wind conditions, it is quite interesting to investigate why the CI occurrence in the plain region is remarkably more prevalent in the
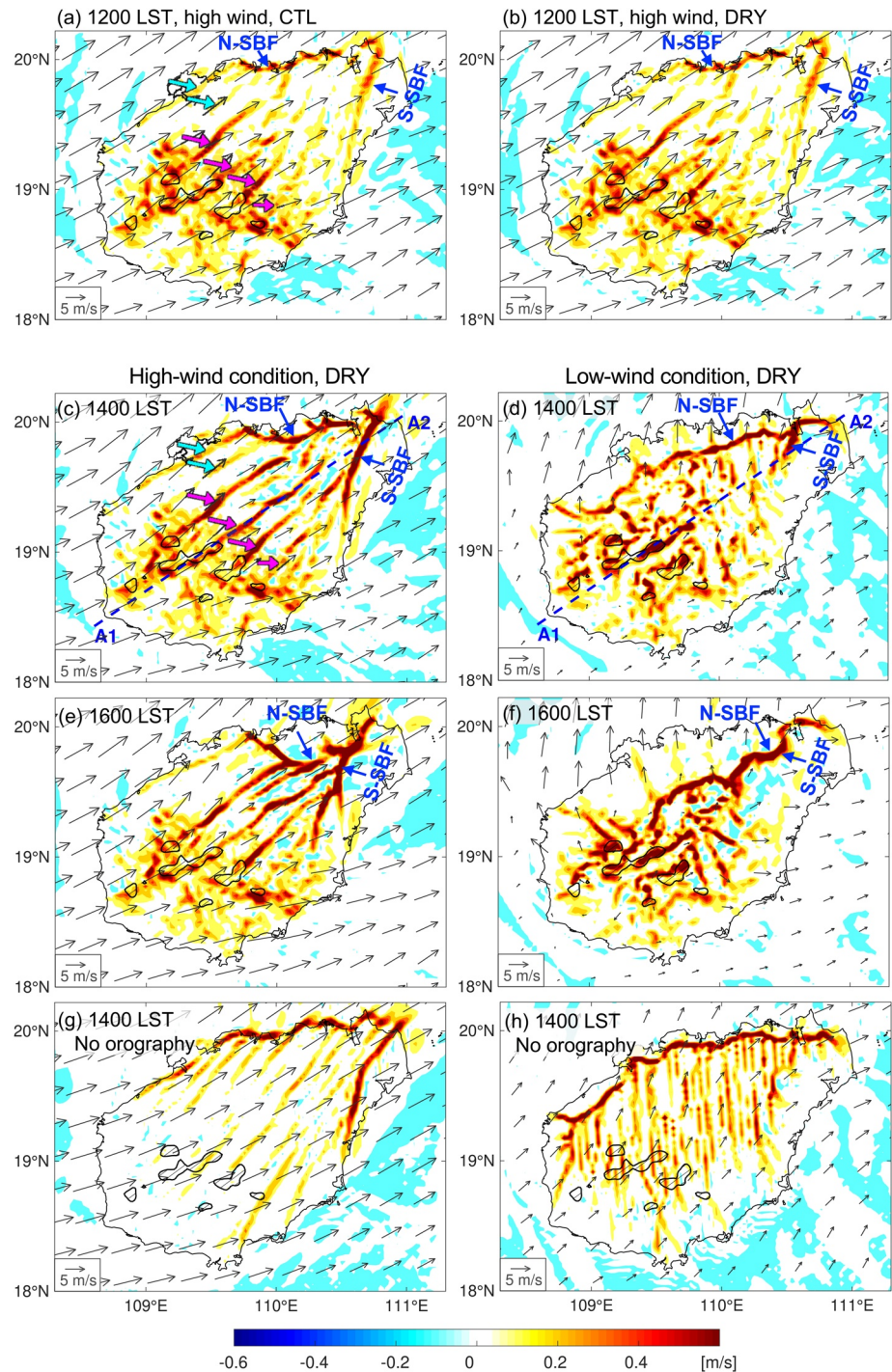
Figure 4. Max vertical motions (shaded; units: m s^{-1}) in the lowest 2 km above ground level with the horizontal wind vectors on 850 hPa. The hatched area within the contours indicates the terrain at an altitude of above 850 m, indicating the locations of mountain ridges. The panels (a and b) represent the high-wind condition in the CTL and DRY simulations, respectively. The panels (c and e) and (d and f) represent the high-wind and low-wind conditions in the DRY simulations, respectively. The blue arrows denote the sea-breeze fronts on the northwest (N-SBF) and southeast (S-SBF) coast. The magenta and cyan arrows denote the enhanced and nonenhanced horizontal convective rolls, respectively. (g and h) Same as (c and d) but for the simulations without mountains. For reference, the original mountain ridges are also plotted by the hatched area. The dashed blue line (A1–A2) represents the location for plotting the vertical cross sections in Figure 5.
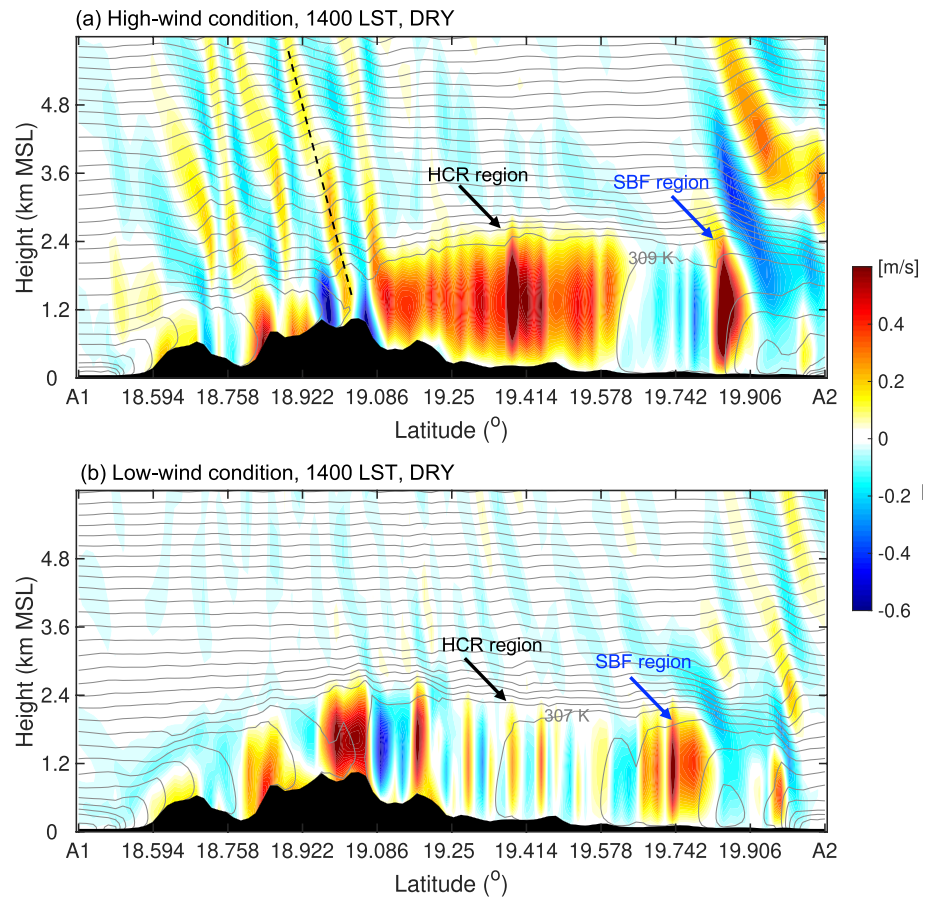
Figure 5. Vertical cross sections of vertical motions (shaded; units: m s^{-1}) and isentropes (isopleths; contour interval = 1 K) during (a) high-wind and (b) low-wind conditions along the dashed blue lines A1–A2 as shown in Figures 4c and 4d. The results are obtained from the DRY simulations. The dashed black line in (a) denotes the tilt of updraft motion as described in the text.

high-wind condition in contrast to that in the low-wind condition (Figures 2c and 2d). In the DRY experiment, the enhanced convergent zones downwind of the ridges are HCRs that intersect the SBFs from the northwest and southeast coasts in the high-wind condition (Figures 4c and 4e). The interaction between these enhanced HCRs and SBFs tends to produce a stronger lift than the SBF collision alone, which leads to a higher probability for CI. Additional dry simulations without orography (DRY_NO_TER in Table S1) were also conducted. During the high-wind condition in DRY_NO_TER, the HCRs in southwest-northeast orientation are still present on the island but with weaker updrafts in the boundary layer (Figure 4g). It seems that the HCRs that form downstream of the mountain ridges tend to be intensified relative to the DRY_NO_TER HCRs.

The connection in the spatial dependence between these enhanced HCRs and ridges also indicates that the ridges stimulate the HCR formation and growth in the high-wind condition. Figure 5a shows that the isentropes downstream of the major ridges do not show an apparent wave pattern like that over the mountains, suggesting that the formation of HCRs is less connected to orographic gravity waves. For a typical gravity-wave signal, the wave crests of upward motion are expected to be more-or-less parallel to the main terrain feature and perpendicular to the low-level flow. In the current case, the lee-side wave pattern of upward motion in the lowest 2.4 km layer is nearly parallel to the low-level flow and is thus actually the nature of HCR (Figures 4c and 5a). The dynamic disturbances (e.g., convergence or wake vortices) at the lees of orographic obstacles combined with the warm land surface condition during the daytime ultimately control the formation and growth of these enhanced HCRs downwind of the ridges as a convective boundary layer develops.

In the low-wind condition, the DRY experiment shows that the updraft motions on the lees of the orography seem to be disorganized (Figures 4d and 4f). No enhanced HCR is located downwind of the mountain ridges. Due to the lack of the enhanced and organized lee-side HCRs, the probability for CI tends to be lower than that in the high-wind condition over the northeast portion of Hainan Island. Additionally, the island region in the low-wind condition is characterized by the southerly near-ground flows (not shown), which leads to no easily identifiable thin-line feature (e.g., horizontal convergence of SBF) on the southern coasts (Figure 4d). Nevertheless, the collision of sea breezes from the northeast and northwest coasts can also be located over the northeast part of the island (Figures 4d and 4f), producing the enhanced forced lifting for CI in that region (Figures 3b, 3d and 3f). Under the influence of orography, the HCR formation over the flat terrain is also not readily noticeable. After the orography being artificially removed (DRY_NO_TER), the HCRs tend to form in the south-north direction (Figure 4h) as a result of the meridionally oriented shear vector in convective boundary layer in the low-wind condition (not shown; Weckwerth et al., 1997).

Although the enhanced and organized HCRs are relatively hard to develop in the low-wind condition, strong thermals exist over the mountain regions (Figures 4d, 4f and 5b). Previous studies have suggested that the convective activity in the mountain area of an island during low-wind conditions is primarily dominated by local thermal circulations. Owing to the different heat capacities between the ocean and the tropical island, the island is heated much faster than the surrounding ocean, resulting in the collisions of sea-breeze fronts from different sides of the island (Zhu et al., 2017). Within the relatively lower-speed low-level flows, the rising motions induced by orography and surface heating are less tilted, which favors CI by providing air parcels with sustained lift at low levels (e.g., Markowski et al., 2006). By contrast, in the high-wind condition, the orography-induced updrafts over the mountains extend to higher levels with the phase of maximum upward motion tilting upstream (or westward) with height (refer to the dashed line in Figure 5a; e.g., Durran, 1990). Such upstream tilts of updraft and downdraft motions may suppress the rising of surface-based air parcels at higher levels, because the trajectories of air parcels tilt downstream (or eastward) with increasing height within ambient southwesterlies on low levels. On this aspect, the rising air parcels in the low-wind condition tend to be less suppressed at higher levels over the mountains in contrast to those in the high-wind condition, suggesting a higher probability for CI in this region in the low-wind condition.

The above analyses demonstrate that the lifting associated with the interaction between SBFs and the enhanced HCRs downwind of the mountain ridges is responsible for the daytime CI hotspot over the northeast plains in the high-wind condition (Figures 2c and 4c, 4e). The existences of these enhanced HCRs to some extent determine the occurrence of convection along HCRs, which is confirmed on a high-wind day by satellite observations (Figure 1b). In the low-wind condition, the thermals that are primarily induced by surface heating and the N-SBF approaching the mountains are responsible for the daytime CI hotspot in the mountain areas (Figures 2d and 4d, 4f). The SBF collision also contributes to the dynamic lifting for CI in the low-wind condition, which is responsible for the secondary CI hotspot over the northeast coastal region in the day (Figure 2d).

5. Summary and Conclusions

The influence of the large-scale low-level wind speed on the spatial distribution of convection triggering over Hainan Island, a tropical island in South China, was examined with the aid of a 3-years radar climatology and numerical simulations. The study period was focused on the first rainy season (April–June) when the island region is characterized by prevailing low-level southwesterlies. During high-wind conditions, the daytime convection initiates most prominently on the lee-side plains of mountain ridges while convection over mountains tends to be inhibited. During low-wind conditions, however, the CI hotspot is preferentially located over mountains, with less frequent CI occurrences over the plain region.

Numerical simulations driven by the average atmospheric conditions were conducted to gain insight into the mechanisms of such CI patterns during the high-wind and low-wind conditions. Results show that the major mountain ridges tend to disturb the low-level flow with high wind and thus control the formation and growth of enhanced HCRs downwind of these ridges. These HCRs subsequently intersect with the SBFs over the plains, further intensifying the low-level convergence which contributes to the convection triggering in that region. The findings complement our traditional understandings in which the sea-breeze

collision is primarily responsible for the convection on the plains of this island. Considering that large-scale circulations now can be predicted reasonably well by numerical models, these findings may be an important reference for the forecast of island thunderstorms.

This study was restricted to quasi-idealized scenarios in which the atmospheric conditions were derived from mean flows. Additional perfectly idealized scenarios would be also worthwhile to separately study the influence of the spatial scale, shape, orientation, and topography of the island on the activities of horizontal convective rolls and sea breezes (e.g., Dailey & Fovell, 1999; Fovell & Dailey, 2001). Another interesting topic is the dominant triggering mechanisms of the nocturnal convection on the southwest coasts of Hainan Island, which waits for further investigation.

Conflict of Interest

No author of this manuscript has a conflict of interest to declare.

Data Availability Statement

The radar-based data for generating Figure 2 and the WRF run-files are available at https://zenodo.org/record/4703188. The ERA-Interim reanalysis produced by ECMWF can be downloaded from https://rda.ucar.edu/datasets/ds627.0/

References

Bai, L., Chen, G., & Huang, L. (2020a). Convection initiation in monsoon coastal areas (South China). *Geophysical Research Letters*, *47*, e2020GL087035. https://doi.org/10.1029/2020GL087035

Bai, L., Chen, G., & Huang, L. (2020b). Image processing of radar mosaics for the climatology of convection initiation in South China. *Journal of Applied Meteorology and Climatology*, *59*, 65–81. https://doi.org/10.1175/JAMC-D-19-0081.1

Bai, L., Meng, Z., Huang, Y., Zhang, Y., Niu, S., & Su, T. (2019). Convection initiation resulting from the interaction between a quasi-stationary dryline and intersecting gust fronts: A case study. *Journal of Geophysical Research: Atmospheres*, *124*, 2379–2396. https://doi.org/10.1029/2018JD029832

Bao, X., & Zhang, F. (2013). Impacts of the mountain-plains solenoid and cold pool dynamics on the diurnal variation of warm-season precipitation over northern China. *Atmospheric Chemistry and Physics*, *13*, 6965–6982. https://doi.org/10.5194/acp-13-6965-2013

Bennett, L. J., Browning, K. A., Blyth, A. M., Parker, D. J., & Clark, P. A. (2006). A review of the initiation of precipitating convection in the United Kingdom. *Quarterly Journal of the Royal Meteorological Society*, *132*, 1001–1020. https://doi.org/10.1256/qj.05.54

Boybeyi, Z., & Raman, S. (1992). A three-dimensional numerical sensitivity study of convection over the Florida peninsula. *Boundary-Layer Meteorology*, *60*(4), 325–359. https://doi.org/10.1007/BF00155201

Carbone, R. E., Wilson, J. W., Keenan, T. D., Hacker, J. M., & Hacker, J. M. (2000). Tropical island convection in the absence of significant topography. Part I: Life cycle of diurnally forced convection. *Monthly Weather Review*, *128*, 3459–3480. https://doi.org/10.1175/1520-0493(2000)128<3459:ticita>2.0.co;2

Chen, J., Cai, X., Wang, H., Kang, L., Zhang, H., Song, Y., et al. (2018). Tornado climatology of China. *International Journal of Climatology*, *38*, 2478–2489. https://doi.org/10.1002/joc.5369

Chen, X., Zhang, F., & Zhao, K. (2016). Diurnal variations of the land-sea breeze and its related precipitation over South China. *Journal of the Atmospheric Sciences*, *73*(12), 4793–4815. https://doi.org/10.1175/jas-d-16-0106.1

Chen, X., Zhang, F., & Zhao, K. (2017). Influence of monsoonal wind speed and moisture content on intensity and diurnal variations of the Mei-Yu season coastal rainfall over South China. *Journal of the Atmospheric Sciences*, *74*(9), 2835–2856. https://doi.org/10.1175/JAS-D-17-0081.1

Chou, M.-D., & Suarez, M. J. (1994). An efficient thermal infrared radiation parameterization for use in general circulation models. *NASA Tech. Memo, NASA*, 84.

Crook, N. A. (2001). Understanding hector: The dynamics of island thunderstorms. *Monthly Weather Review*, *129*, 1550–1563. https://doi.org/10.1175/1520-0493(2001)129<1550:uhtdoi>2.0.co;2

Dailey, P. S., & Fovell, R. G. (1999). Numerical simulation of the interaction between the sea-breeze front and horizontal convective rolls. Part I: Offshore ambient flow. *Monthly Weather Review*, *127*, 858–878. https://doi.org/10.1175/1520-0493(1999)127<0858:NSOTIB>2.0.CO;2

Doswell, C. A., Brooks, H. E., & Maddox, R. A. (1996). Flash flood forecasting: An ingredients-based methodology. *Weather and Forecasting*, *11*, 560–581. https://doi.org/10.1175/1520-0434(1996)011<0560:fffaib>2.0.co;2

Durran, D. R. (1990). Mountain waves and downslope winds. In W. Blumen (Ed.), *Atmospheric processes over complex terrain*. Meteorological monographs (Vol. 23, pp. 59–81). Boston, MA: American Meteorological Society. https://doi.org/10.1007/978-1-935704-25-6_4

Fabry, F., Cazenave, Q., & Basivi, R. (2013). 10.1 Echo climatology, impact of cities, and initial convection studies: New horizons opened using 17 years of conterminous US radar mosaics. Paper presented at 36th Conference on Radar in MeteorologyBreckenridge: American Meteorological Society. Retrieved from https://ams.confex.com/ams/36Radar/webprogram/Paper228783.html

Fovell, R. G. (2005). Convective initiation ahead of the sea-breeze front. *Monthly Weather Review*, *133*, 264–278. https://doi.org/10.1175/MWR-2852.1

Fovell, R. G., & Dailey, P. S. (2001). Numerical simulation of the interaction between the sea-breeze front and horizontal convective rolls. Part II: Alongshore ambient flow. *Monthly Weather Review*, *129*, 2057–2072. https://doi.org/10.1175/1520-0493(2001)129<2057:NSOTIB>2.0.CO;2

Hong, S.-Y., Dudhia, J., & Chen, S.-H. (2004). A revised approach to ice microphysical processes for the parameterization of clouds and precipitation. *Monthly Weather Review*, *132*, 103–120. https://doi.org/10.1175/1520-0493(2004)132<0103:aratim>2.0.co;2

Kingsmill, D. E. (1995). Convection initiation associated with a sea-breeze front, a gust front, and their collision. *Monthly Weather Review*, *123*, 2913–2933. https://doi.org/10.1175/1520-0493(1995)123<2913:ciawas>2.0.co;2

Markowski, P. M., Hannon, C., & Rasmussen, E. (2006). Observations of convection initiation "failure" from the 12 June 2002 IHOP deployment. *Monthly Weather Review*, *134*, 375–405. https://doi.org/10.1175/mwr3059.1

Miller, S. T. K., Keim, B. D., Talbot, R. W., & Mao, H. (2003). Sea breeze: Structure, forecasting, and impacts. *Reviews of Geophysics*, *41*, 1011. https://doi.org/10.1029/2003RG000124

Noh, Y., Cheon, W.-G., Hong, S.-Y., & Raasch, S. (2003). Improvement of the K-profile model for the planetary boundary layer based on large eddy simulation data. *Boundary-Layer Meteorology*, *107*, 401–427. https://doi.org/10.1023/a:1022146015946

Qian, J., Robertson, A. W., & Moron, V. (2013). Diurnal cycle in different weather regimes and rainfall variability over Borneo associated with ENSO. *Journal of Climate*, *26*, 1772–1790. https://doi.org/10.1175/JCLI-D-12-00178.1

Qian, T., Epifanio, C. C., & Zhang, F. (2009). Linear theory calculations for the sea breeze in a background wind: The equatorial case. *Journal of the Atmospheric Sciences*, *66*, 1749–1763. https://doi.org/10.1175/2008JAS2851.1

Saito, K., Keenan, T., Holland, G., & Puri, K. (2001). Numerical simulation of the diurnal evolution of tropical island convection over the Maritime Continent. *Monthly Weather Review*, *129*, 378–400. https://doi.org/10.1175/1520-0493(2001)129<0378:nsotde>2.0.co;2

Simpson, J. E. (1994). *Sea breeze and local wind* (p. 234). Cambridge University Press.

Skamarock, W. C., Klemp, J. B., Dudhia, J., Gill, D. O., Barker, D., Duda, M. G., et al. (2008). *A description of the advanced research WRF version 3 (NCAR Tech. Note, NCAR/TN-4751STR, NCAR/MMM)*. (p. 113). https://doi.org/10.5065/D68S4MVH

Trier, S. B., Davis, C. A., & Ahijevych, D. A. (2010). Environmental controls on the simulated diurnal cycle of warm-season precipitation in the continental United States. *Journal of the Atmospheric Sciences*, *67*, 1066–1090. https://doi.org/10.1175/2009JAS3247.1

Wang, C. (2014). *Hainan climatology* (p. 18). China Meteorological Press.

Weckwerth, T. M., & Parsons, D. B. (2006). A review of convection initiation and motivation for IHOP_2002. *Monthly Weather Review*, *134*(1), 5–22. https://doi.org/10.1175/mwr3067.1

Weckwerth, T. M., Wilson, J. W., Hagen, M., Emerson, T. J., Pinto, J. O., Rife, D. L., & Grebe, L. (2011). Radar climatology of the COPS region. *Quarterly Journal of the Royal Meteorological Society*, *137*, 31–41. https://doi.org/10.1002/qj.747

Weckwerth, T. M., Wilson, J. W., Wakimoto, R. M., & Crook, N. A. (1997). Horizontal convective rolls: Determining the environmental conditions supporting their existence and characteristics. *Monthly Weather Review*, *125*, 505–526. https://doi.org/10.1175/1520-0493(1997)125<0505:HCRDTE>2.0.CO;2

Wilson, J. W., & Roberts, R. (2006). Summary of convective storm initiation and evolution during IHOP: Observational and modeling perspective. *Monthly Weather Review*, *134*, 23–47. https://doi.org/10.1175/mwr3069.1

Zhang, Q., Ni, X., & Zhang, F. (2017). Decreasing trend in severe weather occurrence over China during the past 50 years. *Scientific Reports*, *7*, 42310. https://doi.org/10.1038/srep42310

Zhang, Y., Sun, J., & Fu, S. (2014). Impacts of diurnal variation of mountain-plain solenoid circulations on precipitation and vortices east of the Tibetan Plateau during the Mei-Yu season. *Advances in Atmospheric Sciences*, *31*, 139–153. https://doi.org/10.1007/s00376-013-2052-0

Zheng, Y., Xue, M., Li, B., Chen, J., & Tao, Z. (2016). Spatial characteristics of extreme rainfall over China with hourly through 24-hour accumulation periods based on national-level hourly rain gauge data. *Advances in Atmospheric Sciences*, *33*, 1218–1232. https://doi.org/10.1007/s00376-016-6128-5

Zhu, L., Chen, X., & Bai, L. (2020). Relative roles of low-level wind speed and moisture in the diurnal cycle of rainfall over a tropical island under monsoonal flows. *Geophysical Research Letters*, *47*, e2020GL087467. https://doi.org/10.1029/2020GL087467

Zhu, L., Meng, Z., Zhang, F., & Markowski, P. M. (2017). The influence of sea- and land-breeze circulations on the diurnal variability in precipitation over a tropical island. *Atmospheric Chemistry and Physics*, *17*, 13213–13232. https://doi.org/10.5194/acp-17-13213-2017